Research Square

Preprints are preliminary reports that have not undergone peer review.
They should not be considered conclusive, used to inform clinical practice,
or referenced by the media as validated information.

Inflammation-driven bone erosion and reactive remodeling in experimental arthritis revealed by cortical bone surface analysis

Anders Nguyen
University of Gothenburg
David A. McBride
Calibr-Skaggs Institute for Innovative Medicines, The Scripps Research Institute
Miriam Bollmann
University of Gothenburg
Liam Davidsson
University of Gothenburg
Nour Dada
University of Gothenburg
Lisi Wagener
University of Gothenburg
Muhammad Arif
University of Gothenburg
Linda C. Johansson
University of Gothenburg
Mattias N. D. Svensson
mattias.svensson@rheuma.gu.se
University of Gothenburg

Research Article

Keywords: micro-computed tomography, rheumatoid arthritis, cortical bone erosions, bone remodeling, RANKL

Posted Date: March 30th, 2026

DOI: https://doi.org/10.21203/rs.3.rs-9210680/v1

License: This work is licensed under a Creative Commons Attribution 4.0 International License.
Read Full License

Additional Declarations: No competing interests reported.

Version of Record: A version of this preprint was published at Arthritis Research & Therapy on August 6th, 2026. See the published version at https://doi.org/10.1186/s13075-026-03874-y.

Abstract

Background

Pre-clinical models of inflammatory arthritis are widely used to investigate mechanisms of disease pathology and evaluate therapeutic interventions. However, the sequence of inflammatory activation, bone erosion and reactive bone remodeling remains incompletely defined. We therefore sought to define the time-dependent relationship between inflammation and structural bone remodeling in experimental arthritis.

Methods

K/BxN serum-transfer–induced arthritis was induced in C57BL/6J mice, with longitudinal assessment of clinical disease, histopathology, joint gene expression and structural bone changes during disease progression. µCT analyses included semi-quantitative scoring, conventional morphometric parameters and BRAVO, our in-house µCT-based cortical surface roughness analysis workflow. Anti-RANKL treatment was used to evaluate therapeutic modulation of structural outcomes.

Results

Synovial inflammation preceded histologically detectable cartilage depletion and bone erosion. Transcriptional activation of inflammatory and osteoclast-associated genes defined a pre-erosive molecular phase preceding measurable structural damage, whereas osteoblast- and matrix remodeling–associated genes increased during the reparative phase. Conventional µCT morphometrics and BRAVO both captured the overall erosive trajectory. However, BRAVO demonstrated greater sensitivity, improved reproducibility and age stability, and more clearly resolved distinct erosive and remodeling phases across disease progression. Anti-RANKL treatment significantly reduced cortical bone erosions, and these structural effects were detected by BRAVO but not by conventional morphometric analysis.

Conclusion

By integrating longitudinal gene expression profiling with high-resolution structural analysis, this study defines coordinated phases of inflammation-driven bone damage and reactive bone formation in experimental inflammatory arthritis. BRAVO provides a sensitive approach for quantifying erosive pathology and evaluating therapeutic effects on structural outcomes.

Introduction

Rheumatoid arthritis (RA) is a chronic inflammatory disease characterized by persistent synovial inflammation that drives progressive structural joint damage (1, 2). Cartilage depletion and bone

erosions can occur early in the disease and represents defining features of RA, contributing substantially to long-term disability. Although erosive lesions may undergo partial repair under effective anti-rheumatic therapy, complete structural restoration is uncommon, and new erosions can develop despite apparent inflammatory control (3–7). Together, these observations emphasize the importance of early, sensitive detection of erosive change to guide timely, targeted therapeutic interventions aimed at preventing progressive bone damage and promoting structural repair.

Mechanistically, structural progression in RA reflects a sustained imbalance between bone resorption and insufficient repair, predominantly driven by inflammation-induced osteoclastogenesis and osteoclast-mediated bone resorption (8). The cytokine- and chemokine-rich synovium promote leukocyte recruitment, stromal cell activation and production of matrix-degrading enzymes, while receptor activator of nuclear factor κB ligand (RANKL), a key regulator of osteoclastogenesis, provides a mechanistic link between inflammation and bone resorption (9–12).

Experimental arthritis models have been instrumental in uncovering mechanisms of joint inflammation and structural damage. They provide a controlled setting to dissect how synovial inflammation, bone erosion and subsequent bone repair evolve over time and to link these processes to underlying molecular programs. High-resolution micro-computed tomography (μCT) enables three-dimensional visualization of erosive bone lesions and is widely used in experimental arthritis (13–16). However, erosion severity is often assessed by observer-based scoring or global morphometric parameters that may miss subtle erosive changes and can be influenced by physiological or reparative bone growth, complicating interpretation across ages and experimental conditions (17–19). More robust structural readouts are therefore needed to quantify these processes across disease stages and to validate osteoclast-targeting interventions.

To address this need, we developed BRAVO (Bone Roughness Analysis and Visualization Operator), a μCT-based analysis workflow designed to quantify alterations in the cortical bone surface as a readout of erosive lesions. Here, we combined BRAVO with histopathology and kinetic gene expression profiling in the K/BxN serum-transfer-induced arthritis (STIA) model to define the time-dependent relationship between synovial inflammation and structural damage and to define erosive and reparative phases during disease progression.

Materials and methods

Mice, K/BxN serum-transfer arthritis and treatment

Male C57BL/6J mice were obtained from Janvier Labs. STIA was induced as previously described using serum from arthritic K/BxN mice (20, 21). Disease progression was monitored three times per week from the day of serum injection by clinical scoring of wrists and ankles on a scale from 0 to 4 and by measurement of ankle swelling as described previously (22). For detailed information regarding the STIA model see supplementary material.

For treatment studies, mice received intraperitoneal (i.p.) injections of either 125 µg anti-mouse RANKL antibody (clone IK22/5, BioXcell) or the corresponding rat IgG2a isotype control (clone 2A3, BioXcell) as indicated in the figure legends.

Mice were housed under standard conditions (12-hour light/dark cycle, 21°C, 48% humidity) with food and water provided ad libitum. All animal experiments were conducted at the Laboratory for Experimental Biomedicine, University of Gothenburg, in accordance with approved ethical protocols (5.8.18–09076/2020 and 5.8.18–07352/2025).

Micro-computed tomography (µCT) acquisition and reconstruction

Hind paw joints were fixed in 4% formalin for 72 hours, stored in 70% ethanol, and rehydrated in PBS for 24 hours before scanning. Samples were imaged using a Skyscan 1176 µCT system (Bruker) at a voxel size of 9 µm, with scanning parameters of 54 kV, 467 µA, and a 0.2-mm aluminum filter. Each sample was exposed for 880 ms, with X-ray projections acquired at 0.42° intervals over a 180° rotation using four-frame averaging. Three-dimensional datasets were reconstructed using NRecon software (version 1.6.9.8, Bruker) and DataViewer (version 1.5.0.9, Bruker). Quantitative analyses were performed using CT-Analyzer software (version 1.14.4.1, Bruker), and three-dimensional visualizations used for semi-quantitative scoring were generated using CTVox (version 2.7, Bruker). For detailed information regarding µCT scanning see supplementary material.

Semi-quantitative µCT scoring of bone erosion and formation

Bone erosion and bone formation were assessed using an observer-based semi-quantitative assessment of three-dimensional µCT scans, following an established scoring system (23, 24). The hind paw was divided into two regions: (i) the full hind paw, including the calcaneus, centrale, distal tarsals, astragalus, distal tibia and fibula, and metatarsals, and (ii) the isolated calcaneus. Phalanges and claws were excluded due to minimal erosion in these regions. Scoring information is provided in the supplementary material.

Quantitative µCT morphometric analysis and erosive morphology index (EMI)

Quantitative µCT morphometric parameters were assessed using CT-Analyzer software, including bone surface area (SA), reflecting the outer cortical surface, and bone volume (BV), representing total bone volume. The erosive morphology index (EMI), was calculated as the ratio of surface area to bone volume (EMI = SA/BV), as previously described (25, 26), providing a normalized measure of cortical bone surface area relative to total bone volume.

BRAVO-based cortical bone surface roughness analysis

To quantify arthritis-associated changes in the outer cortical bone surface, we applied a surface-based analysis approach using our in-house Bone Roughness Analysis and Visualization Operator (BRAVO) MATLAB workflow, which was adapted from previously established methods (16, 27). Following reconstruction of three-dimensional bone surfaces from µCT datasets, local surface irregularities were assessed by analyzing angular deviations between adjacent surface elements. Distributions of angular deviations were visualized as histograms, and erosion-associated surface irregularities (SI) were quantified as the area under the curve (AUC) above a defined angular threshold (T > 60°).

To enable quantitative comparison across samples and to account for differences in surface size, the AUC (T > 60°) was normalized to the total number of analyzed local surface regions (Surface Area Units [SAU]), yielding a global bone surface roughness metric. All analyses were implemented using an automated, in-house MATLAB workflow optimized for calcaneus bone analysis. Detailed computational procedures are provided in the supplementary material.

RNA isolation, qPCR and gene expression analysis

Collected hind paws were flash-frozen in liquid nitrogen. Samples were homogenized in TRIzol reagent (Invitrogen, Cat. #15596018) using a FastPrep-24 5G instrument (MP Biomedicals). Total RNA was extracted using the PureLink™ RNA Mini Kit (Invitrogen) following the manufacturer's protocol for TRIzol-based isolation. Complementary DNA (cDNA) was synthesized using the iScript™ cDNA Synthesis Kit (Bio-Rad).

Quantitative PCR (qPCR) was performed on a QuantStudio™ 6 Pro Real-Time PCR System (Applied Biosystems) using gene-specific primers and SsoAdvanced Universal SYBR Green Supermix (Bio-Rad). See supplementary table 1 for primer sequences. Each reaction was run in technical duplicates and gene expression levels were normalized (ΔCt calculation) to the housekeeping gene *Gapdh*.

Histopathology

The same hind paws that were previously analyzed by µCT were subsequently decalcified and embedded in paraffin for histological processing. Paraffin-embedded hind paws were sectioned sagittally to an appropriate depth in accordance with SMASH guidelines (28) and stained with either haematoxylin and eosin (H&E) or toluidine blue (TB) using standard histological procedures. Histopathological scoring was performed as previously described (22, 26). Briefly, synovial inflammation and bone erosion was assessed in H&E-stained sections using a semiquantitative scale from 0 to 4. Synovial inflammation was scored based on the extent of inflammatory cell infiltration in the periarticular region: 0 = normal; 1 = minimal infiltration; 2 = mild infiltration; 3 = moderate infiltration; and 4 = marked infiltration. Bone erosion was scored on a scale from 0 to 4: 0 = normal, intact bone; 1 = minimal superficial cortical erosions; 2 = localized subchondral erosions with partial cortical penetration; 3 = extensive cortical and trabecular

bone erosion with pannus invasion and near-complete cortical breakthrough; and 4 = severe bone destruction with full-thickness cortical defects and marked trabecular bone loss.

Cartilage depletion was evaluated using TB-stained sections and scored from 0 to 4: 0 = no cartilage damage with complete matrix staining; 1 = localized cartilage erosions; 2 = more extensive erosions; 3 = severe erosions; and 4 = complete cartilage loss. All histological analyses were performed in a blinded manner. Slides were digitized using a Zeiss Axioscan 7 slide scanner (Zeiss) and analyzed using Zen software (Zeiss).

Statistical analysis

Sample sizes were based on prior experience with C57BL/6J mice to ensure adequate power to detect biologically relevant differences. Statistical analyses were performed using GraphPad Prism (Version 11) or R, and all computational analyses were conducted in Python (version 3.12.11).

Group comparisons were performed using the Mann-Whitney U test or Kruskal-Wallis test with appropriate post hoc corrections, as specified in the figure legends. Principal component analysis (PCA) was performed using Orange Data Mining, with selected principal components collectively explaining at least 80% of the total variance. See supplementary material for additional statistical analysis.

Pairwise associations between gene expression and arthritis-related traits (ankle swelling, EMI and BRAVO) were evaluated using Spearman correlation coefficients. Resulting *P* values were adjusted for multiple hypothesis testing using the Benjamini-Hochberg false discovery rate (FDR) procedure. In heatmap visualizations, correlations that did not remain significant after FDR correction ($q \geq 0.05$) are denoted by "¬*". For time-course analyses, ΔΔCt values were calculated relative to non-arthritic controls and averaged across mice at each time-point to generate gene-level mean expression trajectories.

Data are presented as mean ± SEM, as indicated. A two-sided *P* value < 0.05 was considered statistically significant. For analyses involving multiple testing, P values were adjusted using the Benjamini-Hochberg false discovery rate (FDR) procedure, with $q \geq 0.05$ considered non-significant.

RESULTS

Kinetic histopathological assessment of joints during progression of K/BxN arthritis

The K/BxN STIA model is a well-established and widely used experimental model of inflammatory arthritis, with distinct features of inflammation-induced cartilage depletion, bone erosions and reactive bone formation and repair (9, 18, 29, 30). To characterize the time-dependent relationship between synovial inflammation and structural joint damage, we subjected C57BL/6J mice to STIA (Fig. 1A,B and Supplementary Fig. 1) and performed histopathological assessment of hind paws at different time-points during disease progression. Synovial inflammation was observed already on day 7, preceding the

first detectable signs of bone erosion and cartilage depletion on day 10 (Fig. 1C-F). Synovial inflammation and bone erosion peaked on day 14 and declined progressively until day 28, consistent with inflammatory resolution and bone repair. In contrast, cartilage depletion persisted throughout the disease course, suggesting a lack of cartilage repair (Fig. 1F).

Collectively, these data indicate that synovial inflammation precedes structural joint damage and that cartilage loss can persist despite clinical improvement, mirroring key features of inflammatory arthritis in patients (31).

Three-dimensional µCT assessment of bone remodeling during arthritis progression

To enable three-dimensional assessment of joint-associated bone remodeling, including features that are less readily captured by two-dimensional histology (such as reparative bone formation), we used µCT imaging during STIA progression and resolution and assessed bone erosion and formation in the hind paw and the isolated calcaneus by semi-quantitative scoring (Fig. 2A, Supplementary Fig. 2A,B).

Bone erosion scores peaked on day 14 of STIA in both the hind paw and the calcaneus (Fig. 2B, Supplementary Fig. 2C), with initial signs detected on day 10, consistent with our histopathological findings (Fig. 1E). By comparison, initial signs of bone formation were observed on day 17 post serum injection, approximately three days after peak erosion, and increased progressively to reach maximal levels on day 28 (Fig. 2B, Supplementary Fig. 2D). This sequential pattern is consistent with reparative remodeling occurring as a response to inflammatory bone damage (32, 33).

Notably, erosion and bone formation followed similar time-dependent patterns in both the hind paw and the calcaneus. Accordingly, erosion and formation scores in these regions were strongly correlated (Fig. 2C,D), indicating that the calcaneus reflects overall joint-associated bone remodeling during arthritis. These findings support the use of the calcaneus as a representative bone for µCT-based assessment of bone remodeling in the STIA model.

Implementation of BRAVO for quantitative analysis of arthritis-induced bone erosions

Although semi-quantitative scoring provides an overview of arthritis-associated bone changes, more precise quantitative analyses are needed. Therefore, we performed µCT-based morphometric analyses on the calcaneus to quantify joint-associated bone remodeling during STIA. Conventional morphometric parameters commonly used to quantify arthritis-related changes at the cortical surface (25, 26, 34, 35) were first analyzed, including bone surface area (SA), reflecting the outer cortical surface, bone volume (BV), representing total bone volume, and the derived erosive morphology index (EMI), which normalizes surface area to bone volume (SA/BV) (Fig. 3A,B).

Surface area increased during early disease and peaked on day 14 of STIA, consistent with active erosive remodeling, whereas bone volume increased at later stages, coinciding with disease resolution

and bone formation (Fig. 3C,D Supplementary Fig. 3A). EMI also peaked on day 14 (Fig. 3E), showing a 1.5-fold increase compared with non-arthritic animals (day 0) (Supplementary Fig. 3B), before declining towards non-arthritic control levels by day 28. This pattern closely mirrored semi-quantitative erosion scores (Fig. 2B), confirming that normalization of surface area to bone volume can capture erosion-associated structural changes during STIA progression.

While EMI captured the overall pattern of bone erosion during STIA, the magnitude of change was modest. Therefore, to improve sensitivity to subtle cortical surface alterations, we applied our in-house BRAVO analysis workflow, which quantifies irregularities in otherwise smooth bone surfaces and enables detection of arthritis-associated erosive lesions.

Histogram and heat-map visualizations from BRAVO revealed pronounced surface irregularities (rough areas) during STIA (Fig. 3F,G, Supplementary Fig. 3A). Quantitative BRAVO values were derived by normalizing measures of surface irregularity to the number of analyzed local surface regions (Fig. 3H,I). BRAVO values markedly increased on days 10 and 14 (Fig. 3J), corresponding to 2.0-fold and 4.4-fold increase, respectively, compared with non-arthritic animals (day 0) (Supplementary Fig. 3C). Importantly, BRAVO demonstrated a clearer discrimination between disease stages compared to EMI, indicating greater sensitivity for detecting arthritis-associated cortical bone remodeling.

BRAVO provides robust and age-independent quantification of bone remodeling

To further compare how EMI and BRAVO capture changes in bone remodeling over the course of arthritis, we performed principal component analysis (PCA) separately using key metrics derived from each analysis workflow. PCA of EMI and BRAVO revealed two distinct structural phases during STIA. Early time-points (days 3–7) clustered with non-arthritic controls (day 0 and non-arthritic day 28), whereas samples from peak arthritis (day 14) were distinctly separated along PC1, consistent with maximal bone erosion (Fig. 4A,B). As disease progressed, later time-points (days 17–28) shifted away from the erosion-associated cluster towards a second trajectory, consistent with a transition from bone erosion to bone formation and remodeling. Notably, BRAVO provided improved resolution of disease stages within the remodeling phase, with clear separation of days 10, 14, 17 and 21, whereas these time-points largely overlapped when assessed using EMI (Fig. 4A,B).

BRAVO showed minimal separation between non-arthritic controls on days 0 and 28, indicating that it was less influenced by age-related changes in bone formation compared with EMI (Fig. 4A,B). To assess the influence of age on these analytical approaches, we subjected mature adult mice (33 weeks old), an age at which physiological bone growth is complete (36), to STIA and evaluated bone remodeling on days 14 and 28 post-serum injection (Fig. 4C, Supplementary Fig. 4A,B)

For EMI-derived parameters, bone volume remained largely unchanged between healthy controls and arthritic mice, consistent with limited net bone turnover in mature adult animals (37), whereas surface area, and consequently EMI, was increased on both days 14 and 28 (Fig. 4D,E). The persistent elevation

in surface area on day 28 coincided with increased bone formation detected by semi-quantitative scoring (Supplementary Fig. 4C,E), suggesting that elevated EMI at this time-point reflects bone formation rather than persistent erosions. By comparison, BRAVO-based analysis revealed a marked increase in cortical bone erosions on day 14 that returned to levels comparable to non-arthritic mice by day 28 post-serum injection (Fig. 4F and Supplementary Fig. 4C,D), consistent with erosion scores obtained by semi-quantitative scoring (Supplementary Fig. 4E).

Given the potential age- and bone formation-related influence on EMI, we next evaluated the robustness of EMI and BRAVO by assessing inter-experimental variability and reproducibility across three independent STIA experiments performed 1 to 2 years apart. BRAVO-based analysis demonstrated substantially lower variability than EMI in non-arthritic animals, indicating higher reproducibility across experiments (Fig. 4H-K). The modest variation in BRAVO on day 14 most likely reflects differences in erosive severity between experimental cohorts.

Age-stratified analysis revealed a strong age dependency for EMI, with near-complete separation between young adult and mature adult mice (Fig. 4L). By contrast, BRAVO, exhibited minimal age-related variation, supporting its use as an age-independent structural metric (Fig. 4L). Further evidence for EMI's age dependency was provided by moderate separation within young adult mice but minimal separation among mature adult mice (Supplementary Fig. 4F,G).

Together, these results demonstrate that BRAVO is less influenced by age and experimental variability than EMI and, unlike EMI, can more reliably distinguish cortical bone erosion from subsequent reparative bone formation, establishing it as a robust metric for quantifying bone remodeling in inflammatory arthritis.

Kinetic gene expression profiling characterizes molecular changes during arthritis progression

To complement our structural analysis, we further characterized the molecular programs underlying inflammation-driven bone erosion and subsequent repair by performing kinetic gene expression analysis of arthritic hind paws during STIA (Fig. 5A). Expression of inflammatory mediators (e.g., *Tnf, Il1, Il6*) and leukocyte-recruiting chemokines (e.g., *Ccl5, Cxcl1, Cxcl10*) closely mirrored clinical disease severity, peaking between days 7 and 10 post-serum injection, followed by gradual decline during disease resolution (Fig. 5A, Supplementary Fig. 5A, Supplementary Table 2A). In parallel, osteoclast-associated genes (e.g., *Ctsk* encoding Cathepsin K, *Tnfsf11* encoding RANKL) were upregulated on days 7 and 10 (Fig. 5A, Supplementary Fig. 5B, Supplementary Table 2B), coinciding with peak inflammation and the initiation of bone destruction, before progressively declining during resolution.

Matrix metalloproteinases (MMPs), key mediators of extracellular matrix degradation and joint remodeling (38), also exhibited distinct stage-specific expression patterns (Fig. 5A, Supplementary Fig. 5C, Supplementary Table 2C). *Mmp2, Mmp7* and *Mmp9* were upregulated early in disease, consistent with roles in initiating matrix and cartilage depletion as well as leukocyte and osteoclast recruitment (38,

39), whereas *Mmp3, Mmp10, Mmp12, Mmp13* and *Mmp14* peaked at later stages, aligning with bone remodeling processes and coinciding with measurable changes in cartilage integrity and bone structure (Fig. 1E). In contrast, osteoblast-associated markers (*Alpl* encoding Alkaline phosphatase, *Bglap* encoding Osteocalcin) displayed a delayed expression profile (Fig. 5A, Supplementary Fig. 5B, Supplementary Table 2C), remaining elevated beyond peak clinical arthritis and reaching maximal levels around day 17, consistent with the observed shift towards bone formation (Fig. 2B). Upregulation of type I collagen genes (*Col1a1, Col1a2*) during mid-stage disease coincided with the onset of bone formation and is consistent with activation of matrix deposition in response to inflammatory bone damage.

Importantly, these transcriptional dynamics were closely aligned with disease severity and structural bone changes (Fig. 5A), indicating that gene expression trajectories mirror the progression from initial inflammatory signaling and leukocyte recruitment to bone erosion and cartilage depletion and subsequent bone formation and repair.

Transcriptional programs correlate with clinical severity and structural bone remodeling

To determine how the observed transcriptional changes relate to clinical disease and structural bone remodeling across the arthritis course, Spearman correlation analyses were performed between gene expression levels and arthritis-associated traits and visualized in a gene-trait correlation heatmap (Fig. 5B).

Overall, the genes showing the strongest correlations were predominantly associated with immune cell recruitment, extracellular matrix degradation and bone remodeling, highlighting these processes as prominent features of joint pathology during STIA. Correlations were generally stronger with ankle swelling than with quantitative structural bone metrics, consistent with ankle swelling reflecting cumulative inflammatory activity across the disease course. Notably, EMI and BRAVO showed comparatively stronger associations with bone and matrix remodeling genes than with chemokines, consistent with these metrics capturing tissue remodeling-related outcomes.

Among correlated genes, the chemokines *Cxcl10* and *Ccl5* emerged as strong correlates of ankle swelling, in line with their reported involvement in inflammatory cell recruitment in experimental arthritis(40, 41). Several MMPs also showed robust associations with ankle swelling, consistent with their involvement in extracellular matrix degradation, tissue remodeling and joint destruction during arthritis progression (39, 42, 43).

Within bone remodeling-associated genes, *Tnfsf11* (RANKL), stood out as one of the strongest correlates of disease severity. *Tnfsf11* expression was strongly associated with ankle swelling, consistent with its previously reported elevation in STIA (42, 44). By contrast, *Tnfsf11* showed weak or non-significant correlation with measures of bone erosion. This offset is biologically expected, as transcriptional activation of osteoclast-regulatory pathways precedes the development of measurable bone erosions, meaning that structural metrics such as EMI and BRAVO reflect downstream consequences of

osteoclast activity rather than immediate gene expression. In line with this, structural associations were generally stronger for matrix- and bone turnover-related genes, including matrix-remodeling MMPs (e.g., *Mmp3, Mmp9 and Mmp14*), osteoclast markers (e.g., *Ctsk*) and osteogenic/matrix genes (e.g., *Col1a2, Alpl, Runx2*). Together, these findings indicate that *Tnfsf11* is part of an early transcriptional program associated with clinical disease severity that precedes measurable structural bone changes during STIA.

BRAVO captures treatment-induced suppression of bone erosion during STIA

Given the strong association of *Tnfsf11* with disease severity, we next evaluated whether RANKL inhibition alters inflammation and bone remodeling during STIA (Fig. 6A). Based on the kinetics of *Tnfsf11* expression (Supplementary Fig. 5B), treatment of mice with either a RANKL-targeting antibody or the corresponding isotype control was started three days after STIA induction (Fig. 6A).

Clinical assessment showed that anti-RANKL treatment significantly reduced arthritis severity compared with controls (Fig. 6B,C, Supplementary Fig. 6A,B), which was supported by reduced histopathological signs of synovial inflammation, bone erosion and cartilage depletion (Fig. 6D,E). Semi-quantitative scoring of µCT scans further demonstrated significant reductions in bone erosion on day 14 and subsequent bone formation on day 28 in both the hind paw and the isolated calcaneus following anti-RANKL treatment (Fig. 6F,G, Supplementary Fig. 6C,D).

Quantitative µCT analysis revealed reduced bone erosion on day 14 in anti-RANKL-treated animals using BRAVO (Fig. 6J, Supplementary Fig. 6F), which was supported by BRAVO generated heat maps illustrating reduced presence of erosions (rough areas) in anti-RANKL–treated mice (Fig. 6H). Notably, no significant difference between anti-RANKL-treated and control groups was observed when using EMI analysis (Fig. 6H,I, Supplementary Fig. 6E).

Together, these findings show that RANKL blockade attenuates synovial inflammation and joint destruction and establish BRAVO as a sensitive readout for detecting treatment-induced changes in cortical bone erosion during inflammatory arthritis.

Discussion

Joint destruction is a major cause of long-term disability in RA, and preventing erosive progression remains a key therapeutic goal (4, 43). In this study, we developed and applied BRAVO, a µCT analysis workflow that quantifies cortical bone surface alterations as a sensitive measurement of erosive change during arthritis. Using the K/BxN STIA model, we resolved the time-dependent relationship between synovial inflammation and structural damage, demonstrating that inflammation precedes measurable cartilage and bone destruction and that cartilage loss persists despite clinical improvement. Moreover, anti-RANKL treatment attenuated both disease severity and cortical bone erosions, and these structural effects were detected by BRAVO but not EMI, underscoring the enhanced sensitivity of BRAVO for evaluating osteoclast-targeting interventions.

A major outcome of this work is the performance of BRAVO as a sensitive and robust structural readout of erosive damage. Compared with EMI, which was influenced by age and showed greater inter-experimental variability, BRAVO more reliably detected arthritis-induced cortical bone surface alterations and better separated disease stages and treatment groups. Beyond experimental studies, clinical assessment of erosions by radiography and advanced imaging such as MRI or CT-based techniques is often reported using observer-based semi-quantitative scoring, which may limit sensitivity to subtle erosive progression, requires specialized expertise and is both time- and labor-intensive, introducing potential reader-dependent variability and substantial resource demands (6, 45). A surface-based approach such as BRAVO could, in the future, complement existing imaging readouts by enabling more quantitative assessment of erosive lesions and treatment response.

A prior kinetic study in STIA has profiled joint gene expression during the early inflammatory phase, when clinical scores peak (46). To our knowledge, this is the first study to combine histopathology, quantitative three-dimensional bone assessment and transcriptional profiling across the full course of STIA. This approach outlines a clear sequence of joint pathology in which inflammatory activity and immune cell-recruiting programs peak early, followed by a matrix-degrading and erosive phase and a later shift towards remodeling-associated signatures. By aligning clinical assessments with tissue-level inflammation, structural readouts and gene expression trajectories, our results help guide selection of time-points and endpoints for mechanistic and therapeutic studies, particularly those targeting osteoclast-mediated damage, matrix remodeling or inflammation-driven structural progression.

The osteoclast-inhibiting anti-RANKL antibody denosumab is widely used in the treatment of osteoporosis (47) but is not routinely used for RA. Nevertheless, several clinical studies have found that adding denosumab to conventional anti-rheumatic therapy can limit radiographic erosion progression in RA, with less consistent effects on clinical inflammation or cartilage outcomes (48, 49). In experimental settings, genetic disruption of the RANK-RANKL pathway has likewise been reported to limit structural damage without clearly altering clinical inflammation (9, 11). By contrast, we found that anti-RANKL treatment reduced not only structural damage but also clinical and histological inflammation in STIA, consistent with recent observations in the TNF-transgenic model (50). This could reflect indirect effects of limiting osteoclastogenesis on inflammatory tissue injury and damage-associated signaling, and/or additional RANKL-dependent mechanisms beyond osteoclast differentiation, which will require further study. Importantly, the timing of our intervention was guided by the kinetic profile of *Tnfsf11* expression together with histological and quantitative µCT readouts, enabling treatment to be initiated during the window in which RANKL-associated osteoclastogenic activity was expected to be highest, further highlighting the value of kinetic analyses for optimizing therapeutic study design.

It should be noted that our transcriptional profiling was limited to selected candidate genes and may not capture the full complexity of inflammation-driven bone remodeling. Future studies incorporating broader transcriptomic and proteomic approaches, together with denser sampling during early disease, will be required to more precisely define the molecular programs linking inflammation to structural change. In addition, the STIA model represents an acute, antibody-mediated arthritis and may not fully

recapitulate the chronic synovial pathology of established RA. While we observed a distinct reparative remodeling phase following peak erosion, complete structural restoration is uncommon in patients with RA. Therefore, the reactive bone formation in the STIA model likely reflects remodeling connected to erosion, consistent with limited structural repair observed clinically. Nonetheless, integrating µCT with BRAVO provides a sensitive and reproducible approach for distinguishing active erosive pathology from subsequent reactive remodeling and for quantifying treatment-induced changes in structural damage in experimental inflammatory arthritis.

Conclusion

In this study, we define the time-dependent relationship between synovial inflammation, bone erosion and subsequent remodeling in experimental inflammatory arthritis. By integrating histology, gene expression and µCT-based structural analysis, we show that BRAVO provides a sensitive and robust measure of cortical bone erosions and their response to treatment. These findings highlight the value of combining molecular and structural readouts across disease progression and establish BRAVO as a useful tool for assessing erosive pathology in experimental arthritis models.

Abbreviations

RA
Rheumatoid Arthritis
RANKL
receptor activator of nuclear factor κB ligand
µCT
micro-computed tomography
BRAVO
Bone Roughness Analysis and Visualization Operator
STIA
K/BxN serum-transfer-induced arthritis
i.p.
intraperitoneal
EMI
erosive morphology index
SA
surface area
BV
bone volume
SI
surface irregularities
AUC
area under the curve

SAU
Surface Area Units
cDNA
Complementary DNA
qPCR
Quantitative PCR
H&E
haematoxylin and eosin
TB
toluidine blue
PCA
Principal component analysis
FDR
false discovery rate
SEM
Standard error of mean
IL
Interleukin
TNF
Tumor necrosis factor
CXCL
Chemokine C-X-C motif ligand
CCL
Chemokine C-C motif ligand
MMPs
Matrix metalloproteinases
Tnfsf11
TNF superfamily member 11
Ctsk
Cathepsin K
Alpl
Alkaline phosphatase
Bglap
Bone Gamma-Carboxyglutamate Protein
Col1a1
Collagen Type I Alpha 1 Chain
Col1a2
Collagen Type I Alpha 2 Chain
RUNX2
Runt-related transcription factor 2

Declarations

Ethics approval

All animal experiments were conducted at the Laboratory for Experimental Biomedicine, University of Gothenburg, in accordance with approved ethical protocols (5.8.18-09076/2020 and 5.8.18-07352/2025).

Consent for publication

Not applicable

Availability of data and materials

All data needed to evaluate the conclusions in the paper are present in the paper and/or the Supplementary Materials. Additional data related to this paper may be requested from the authors. The BRAVO MATLAB script will be made available in GitHub upon acceptance of the manuscript

Competing interests

The authors declare that they have no competing interests

Funding

This work was supported by the Swedish Research Council (grants 2025-03125 and 2021-00997 to MNDS and 2019-01891 and 2025-02420 to LCJ), the Swedish Society for Medical Research (grant S19-0062 to MNDS; S19-0121 to LCJ and grant PG-23-0379-H-01 to MB), the Foundation for Research in Rheumatology (FOREUM) to MNDS, The Swedish Rheumatology Association (to MNDS and MB), The Sahlgrenska Academy (to MNDS), the ALF-agreement (ALFGBG-1028985 to MNDS), the King Gustaf V's 80th Anniversary Foundation (to MNDS and MB), Professor Nanna Svartz Research Foundation (to MNDS and MB), Ollie and Elof Ericssons foundation (to MNDS), Apotekare Hedberg Foundation (to MNDS), The Crafoord Foundation (to MB), the Åke Wiberg foundation (to MNDS), the Gunvor och Josef Anérs Foundation (to MNDS), IngaBritt och Arne Lundbergs Research Foundation (to MNDS), the Ragnar Söderberg Foundation (7/22-A to LCJ), the Swedish Foundation for Strategic Research (FFL18-0182 to LCJ) and Knut and Alice Wallenberg Foundation (2021.0065 to LCJ)

Author contributions

MNDS conceived of, designed and supervised the research and wrote the manuscript. A.N and D.A.M developed the BRAVO script, contributed to acquisition and analysis of data and wrote the manuscript. M.B and L.D contributed to acquisition and analysis of data and wrote the manuscript. N.D and LW contributed to acquisition of data. M.A and LCJ provided tools and/or reagents and key scientific input. All authors approved the submitted version of the manuscript.

Acknowledgments

We thank Professor Inger Gjertsson and Associate Professor Cristina Maglio for valuable discussions and insightful feedback on the manuscript.

Data and materials availability:

All data needed to evaluate the conclusions in the paper are present in the paper and/or the Supplementary Materials. Additional data related to this paper may be requested from the authors. The BRAVO MATLAB script will be made available in GitHub upon acceptance of the manuscript

References

1. Alivernini S et al. The pathogenesis of rheumatoid arthritis. *Immunity*. 2022;55(12):2255-2270. doi:10.1016/j.immuni.2022.11.009
2. Smolen JS et al. Rheumatoid arthritis. *The Lancet*. 2016;388(10055):2023-2038. doi:10.1016/S0140-6736(16)30173-8
3. Rauner M et al. Mechanisms of osteoclast activation in inflammatory bone loss in rheumatoid arthritis. *Nat Rev Rheumatol*. 2026;22(1):42-61. doi:10.1038/s41584-025-01323-9
4. Schett G et al. Bone erosion in rheumatoid arthritis: mechanisms, diagnosis and treatment. *Nat Rev Rheumatol*. 2012;8(11):656-664. doi:10.1038/nrrheum.2012.153
5. Smolen JS et al. Tocilizumab inhibits progression of joint damage in rheumatoid arthritis irrespective of its anti-inflammatory effects: disassociation of the link between inflammation and destruction. *Ann Rheum Dis*. 2012;71(5):687-693. doi:10.1136/annrheumdis-2011-200395
6. Gjertsson I et al. Cone Beam Computed Tomography for Assessment of Erosions in Early Rheumatoid Arthritis: A Pilot Study. *J Rheumatol*. 2025;52(8):752-757. doi:10.3899/jrheum.2024-1276
7. Melokhina V et al. Subclinical inflammation and joint damage progression in patients with early RA fulfilling 2011 vs 2022 ACR/EULAR Boolean remission criteria: data from the ARCTIC study. *Ann Rheum Dis*. 2024;83(4):540-541. doi:10.1136/ard-2023-224950
8. Maruotti N et al. Osteoclastogenesis and arthritis. *Clin Exp Med*. 2011;11(3):137-145. doi:10.1007/s10238-010-0117-2
9. Pettit AR et al. TRANCE/RANKL knockout mice are protected from bone erosion in a serum transfer model of arthritis. *Am J Pathol*. 2001;159(5):1689-1699. doi:10.1016/S0002-9440(10)63016-7
10. Gu R et al. Macrophage migration inhibitory factor is essential for osteoclastogenic mechanisms in vitro and in vivo mouse model of arthritis. *Cytokine*. 2015;72(2):135-145. doi:10.1016/j.cyto.2014.11.015
11. Danks L et al. RANKL expressed on synovial fibroblasts is primarily responsible for bone erosions during joint inflammation. *Ann Rheum Dis*. 2016;75(6):1187-1195. doi:10.1136/annrheumdis-2014-207137

12. Dankbar B et al. Myostatin is a direct regulator of osteoclast differentiation and its inhibition reduces inflammatory joint destruction in mice. *Nat Med*. 2015;21(9):1085-1090. doi:10.1038/nm.3917
13. Døhn UM et al. No overall progression and occasional repair of erosions despite persistent inflammation in adalimumab-treated rheumatoid arthritis patients: results from a longitudinal comparative MRI, ultrasonography, CT and radiography study. *Ann Rheum Dis*. 2011;70(2):252-258. doi:10.1136/ard.2009.123729
14. Perry D et al. Detection of erosions in the rheumatoid hand; a comparative study of multidetector computerized tomography versus magnetic resonance scanning. *J Rheumatol*. 2005;32(2):256-267.
15. Hoffmann B et al. Automated Quantification of Early Bone Alterations and Pathological Bone Turnover in Experimental Arthritis by in vivo PET/CT Imaging. *Sci Rep*. 2017;7:2217. doi:10.1038/s41598-017-02389-6
16. Silva MD et al. Application of Surface Roughness Analysis on Micro–Computed Tomographic Images of Bone Erosion: Examples Using a Rodent Model of Rheumatoid Arthritis. *Mol Imaging*. 2006;5(4):7290.2006.00025. doi:10.2310/7290.2006.00025
17. Buttgereit F et al. Transgenic disruption of glucocorticoid signaling in mature osteoblasts and osteocytes attenuates K/BxN mouse serum–induced arthritis in vivo. *Arthritis Rheum*. 2009;60(7):1998-2007. doi:10.1002/art.24619
18. Maleitzke T et al. Transgenic disruption of endogenous glucocorticoid signaling in osteoblasts does not alter long-term K/BxN serum transfer-induced arthritis. *Arthritis Res Ther*. 2023;25(1):140. doi:10.1186/s13075-023-03112-9
19. Døhn UM et al. Rheumatoid arthritis bone erosion volumes on CT and MRI: reliability and correlations with erosion scores on CT, MRI and radiography. *Ann Rheum Dis*. 2007;66(10):1388-1392. doi:10.1136/ard.2007.072520
20. Monach PA et al. The K/BxN arthritis model. *Curr Protoc Immunol*. 2008;Chapter 15:15.22.1-15.22.12. doi:10.1002/0471142735.im1522s81
21. Christensen AD et al. K/BxN Serum-Transfer Arthritis as a Model for Human Inflammatory Arthritis. *Front Immunol*. 2016;7:213. doi:10.3389/fimmu.2016.00213
22. Doody KM et al. Targeting phosphatase-dependent proteoglycan switch for rheumatoid arthritis therapy. *Sci Transl Med*. 2015;7(288):288ra76. doi:10.1126/scitranslmed.aaa4616
23. Croft AP et al. Distinct fibroblast subsets drive inflammation and damage in arthritis. *Nature*. 2019;570(7760):246-251. doi:10.1038/s41586-019-1263-7
24. Antill AC et al. Micro-CT evaluation of rheumatoid arthritis mouse model disease progression: Manual tracings versus semi-automated routines. *Diagn Interv Imaging*. 2016;97(6):651-655. doi:10.1016/j.diii.2015.12.007
25. Andersson KME et al. Down-regulation of survivin alleviates experimental arthritis. *J Leukoc Biol*. 2015;97(1):135-145. doi:10.1189/jlb.3A0714-317R

26. Svensson MND et al. Synoviocyte-targeted therapy synergizes with TNF inhibition in arthritis reversal. *Sci Adv*. 2020;6(26):eaba4353. doi:10.1126/sciadv.aba4353
27. Silva MD et al. Quantitative Analysis of Micro-CT Imaging and Histopathological Signatures of Experimental Arthritis in Rats. *Mol Imaging*. 2004;3(4):15353500200404136. doi:10.1162/15353500200404136
28. Hayer S et al. 'SMASH' recommendations for standardised microscopic arthritis scoring of histological sections from inflammatory arthritis animal models. *Ann Rheum Dis*. 2021;80(6):714-726. doi:10.1136/annrheumdis-2020-219247
29. Jacobs JP et al. Lack of requirement of osteopontin for inflammation, bone erosion, and cartilage damage in the K/BxN model of autoantibody-mediated arthritis. *Arthritis Rheum*. 2004;50(8):2685-2694. doi:10.1002/art.20381
30. Marco-Bonilla M et al. Beyond joints: the importance of animal models in exploring rheumatoid arthritis comorbidities. *Front Med*. 2025;12:1693610. doi:10.3389/fmed.2025.1693610
31. Tateiwa D et al. Cartilage and Bone Destruction in Arthritis: Pathogenesis and Treatment Strategy: A Literature Review. *Cells*. 2019;8(8):818. doi:10.3390/cells8080818
32. Schett G et al. Tumor necrosis factor alpha and RANKL blockade cannot halt bony spur formation in experimental inflammatory arthritis. *Arthritis Rheum*. 2009;60(9):2644-2654. doi:10.1002/art.24767
33. Fardellone P et al. Bone Remodelling Markers in Rheumatoid Arthritis. *Mediators Inflamm*. 2014;2014:484280. doi:10.1155/2014/484280
34. Ozata SK et al. Comparative Micro-CT Evaluation of Ankaferd Blood Stopper, Xenogeneic Grafts, and Their Combination in Bone Healing: An Experimental Study. *J Maxillofac Oral Surg*. Published online December 23, 2025. doi:10.1007/s12663-025-02847-z
35. Donato S et al. Meniscal Ossicles as micro-CT Imaging Biomarker in a Rodent Model of Antigen-Induced Arthritis: a Synchrotron-Based X-ray Pilot Study. *Sci Rep*. 2017;7(1):7544. doi:10.1038/s41598-017-08025-7
36. Somerville JM et al. Growth of C57Bl/6 Mice and the Material and Mechanical Properties of Cortical Bone from the Tibia. *Calcif Tissue Int*. 2004;74(5):469-475. doi:10.1007/s00223-003-0101-x
37. Jilka RL. The Relevance of Mouse Models for Investigating Age-Related Bone Loss in Humans. *J Gerontol A Biol Sci Med Sci*. 2013;68(10):1209-1217. doi:10.1093/gerona/glt046
38. Paiva KBS et al. Chapter Six - Matrix Metalloproteinases in Bone Resorption, Remodeling, and Repair. In: Khalil RA, ed. *Progress in Molecular Biology and Translational Science*. Vol 148. Matrix Metalloproteinases and Tissue Remodeling in Health and Disease: Target Tissues and Therapy. Academic Press; 2017:203-303. doi:10.1016/bs.pmbts.2017.05.001
39. Chia WT et al. MMP-9 mRNA as a Therapeutic Marker in Acute and Chronic Stages of Arthritis Induced by Type II Collagen Antibody. *J Formos Med Assoc*. 2008;107(3):245-252. doi:10.1016/S0929-6646(08)60143-6
40. Lee JH et al. Pathogenic roles of CXCL10 signaling through CXCR3 and TLR4 in macrophages and T cells: relevance for arthritis. *Arthritis Res Ther*. 2017;19:163. doi:10.1186/s13075-017-1353-6

41. Agere SA et al. RANTES/CCL5 Induces Collagen Degradation by Activating MMP-1 and MMP-13 Expression in Human Rheumatoid Arthritis Synovial Fibroblasts. *Front Immunol*. 2017;8. doi:10.3389/fimmu.2017.01341
42. Croft AP et al. Distinct fibroblast subsets drive inflammation and damage in arthritis. *Nature*. 2019;570(7760):246-251. doi:10.1038/s41586-019-1263-7
43. Németh T et al. Synovial fibroblasts as potential drug targets in rheumatoid arthritis, where do we stand and where shall we go? *Ann Rheum Dis*. 2022;81(8):1055-1064. doi:10.1136/annrheumdis-2021-222021
44. Hanaoka R et al. A novel mechanism for the regulation of IFN-gamma inducible protein-10 expression in rheumatoid arthritis. *Arthritis Res Ther*. 2003;5(2):R74-81. doi:10.1186/ar616
45. Sharp JT et al. Variability of precision in scoring radiographic abnormalities in rheumatoid arthritis by experienced readers. *J Rheumatol*. 2004;31(6):1062-1072.
46. Fukushima A et al. Kinetic analysis of synovial signaling and gene expression in animal models of arthritis. *Ann Rheum Dis*. 2010;69(5):918-923. doi:10.1136/ard.2009.112201
47. Miller PD. Denosumab: anti-RANKL antibody. *Curr Osteoporos Rep*. 2009;7(1):18-22. doi:10.1007/s11914-009-0004-5
48. Takeuchi T et al. Effects of the anti-RANKL antibody denosumab on joint structural damage in patients with rheumatoid arthritis treated with conventional synthetic disease-modifying antirheumatic drugs (DESIRABLE study): a randomised, double-blind, placebo-controlled phase 3 trial. *Ann Rheum Dis*. 2019;78(7):899-907. doi:10.1136/annrheumdis-2018-214827
49. So H et al. Effects of RANKL inhibition on promoting healing of bone erosion in rheumatoid arthritis using HR-pQCT: a 2-year, randomised, double-blind, placebo-controlled trial. *Ann Rheum Dis*. 2021;80(8):981-988. doi:10.1136/annrheumdis-2021-219846
50. Papadaki M et al. New Insights for RANKL as a Proinflammatory Modulator in Modeled Inflammatory Arthritis. *Front Immunol*. 2019;10. doi:10.3389/fimmu.2019.00097

Figures

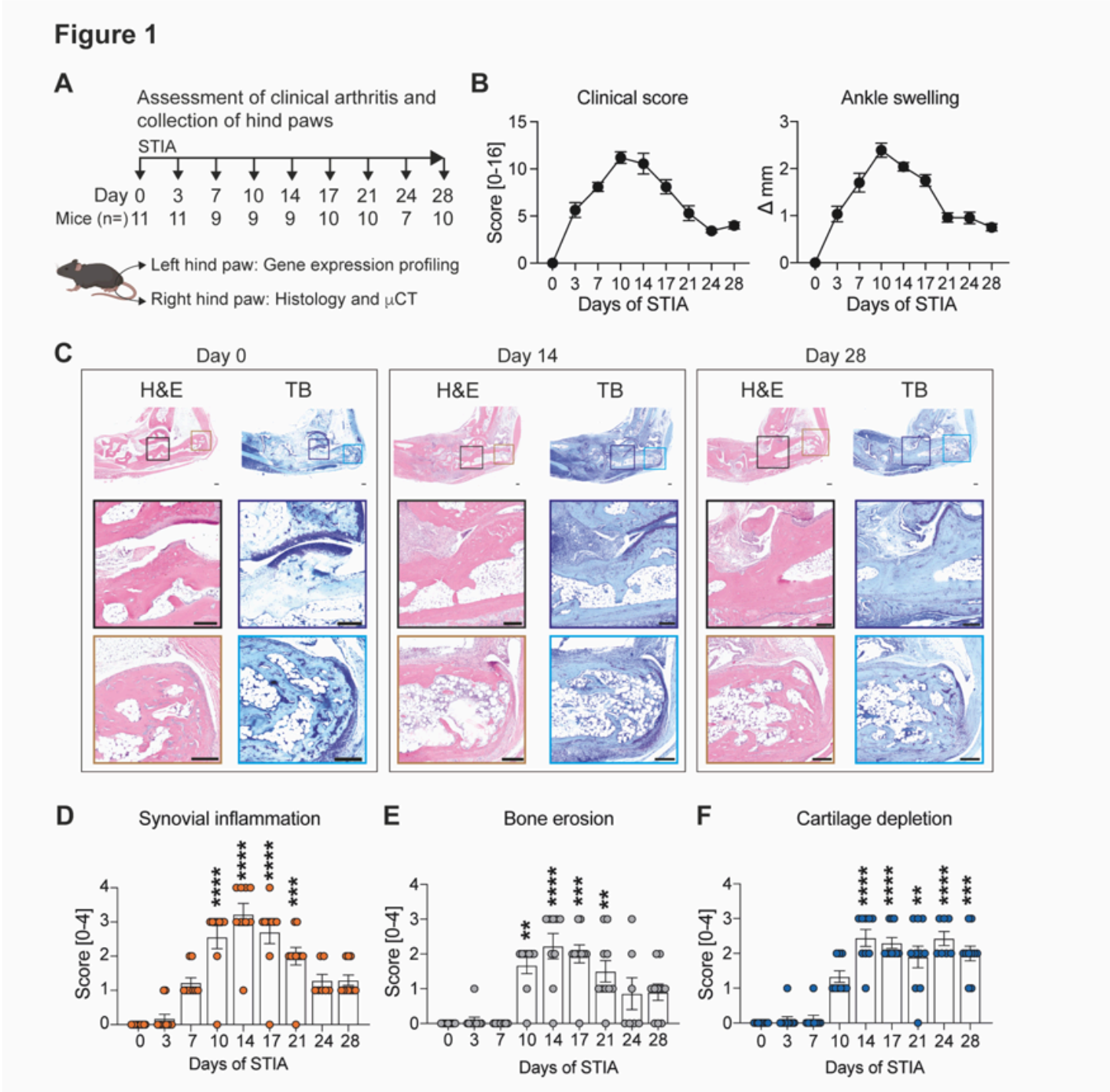


Figure 1

Kinetic assessment of tissue pathology during the course of STIA

A) Schematic overview of the experimental setup indicating time-points for collection of hind paws used in downstream analysis. N equals numbers of mice terminated at each time-point.**B**) Clinical score and ankle swelling in male C57BL/6J mice at different time-points during the course of STIA (n ≥ 7 per group, see **A**). See Supplementary Figure 1 for individual mouse data points. **C**) Representative Haematoxylin and Eosin (H&E) and Toluidine blue (TB) images of hind paws used for histological analysis of synovial

inflammation, bone erosion and cartilage depletion. Scale bars, 200 µm. **D**-**F**) Quantification of synovial inflammation, bone erosion, and cartilage depletion of mice in (**B**). Each symbol in **D**,**E**, and **F** represents an individual mouse. Bars represent mean ± SEM. Statistical significance in **D**-**F**was determined by Kruskal-Wallis test followed by Dunn's multiple comparisons test, with each time point compared to Day 0. ***P* < 0.01, ****P* < 0.001, ****P* < 0.0001.

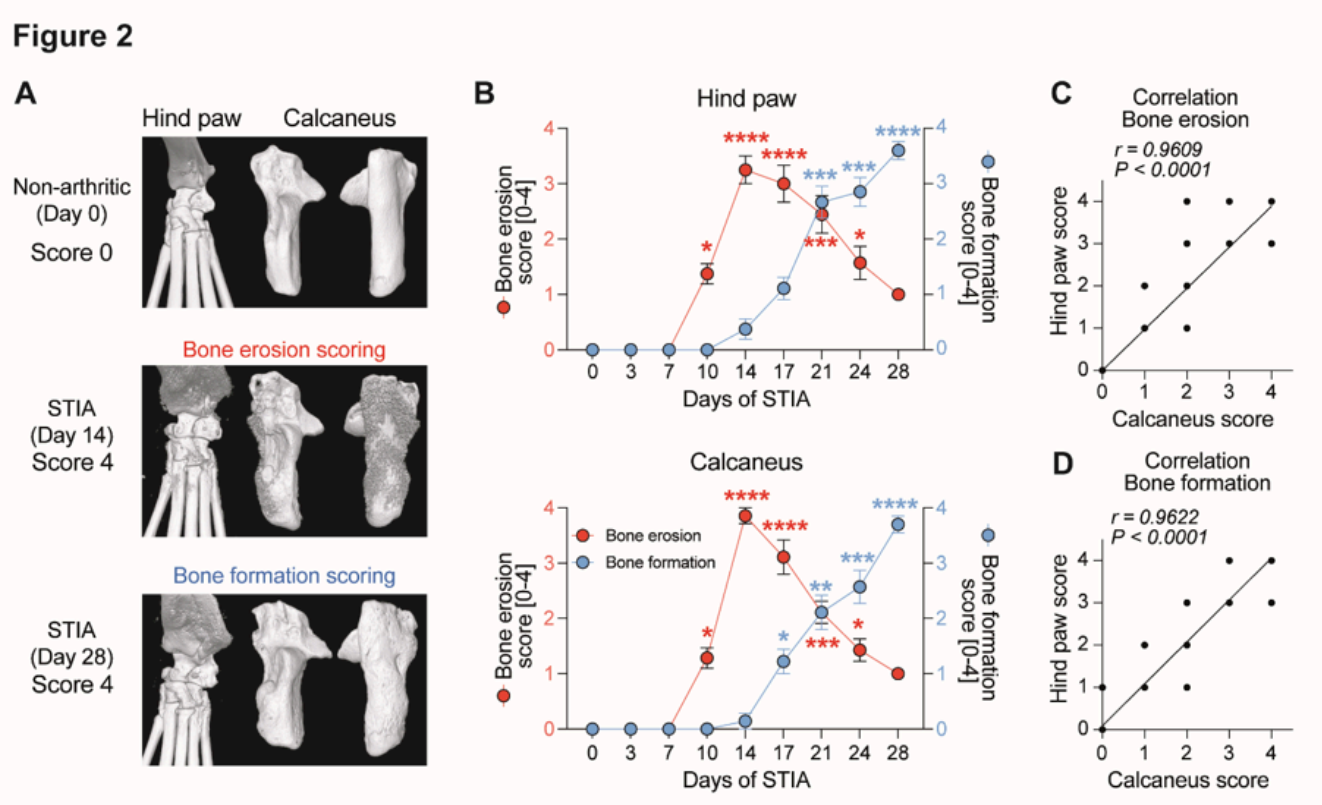


Figure 2

Semi-quantitative scoring of three-dimensional µCT scans reveals distinct phases of bone erosion and formation during STIA

A) Representative images of scoring scale used to assess bone erosion and bone formation in the hind paw and the corresponding calcaneus in the STIA model. See complete scoring scale illustration **in** Supplementary Figure 2A. **B**) Scoring of bone erosion and bone formation in the whole hind paw and the isolated calcaneus at different time-point during STIA (n ≥ 7 per group; see Figure 1A). **C**,**D**) Spearman's correlation analysis between bone erosion and bone formation score between hind-paw and corresponding isolated calcaneus, showing r and two-tailed p values (*P*< 0.0001). Graphs represent means ± SEM. Statistical significance in **B** was determined by Kruskal-Wallis test followed by Dunn's multiple comparisons test, with each time-point compared to Day 0. **P* < 0.05, ***P* < 0.01, ****P* < 0.001, *****P*< 0.0001.

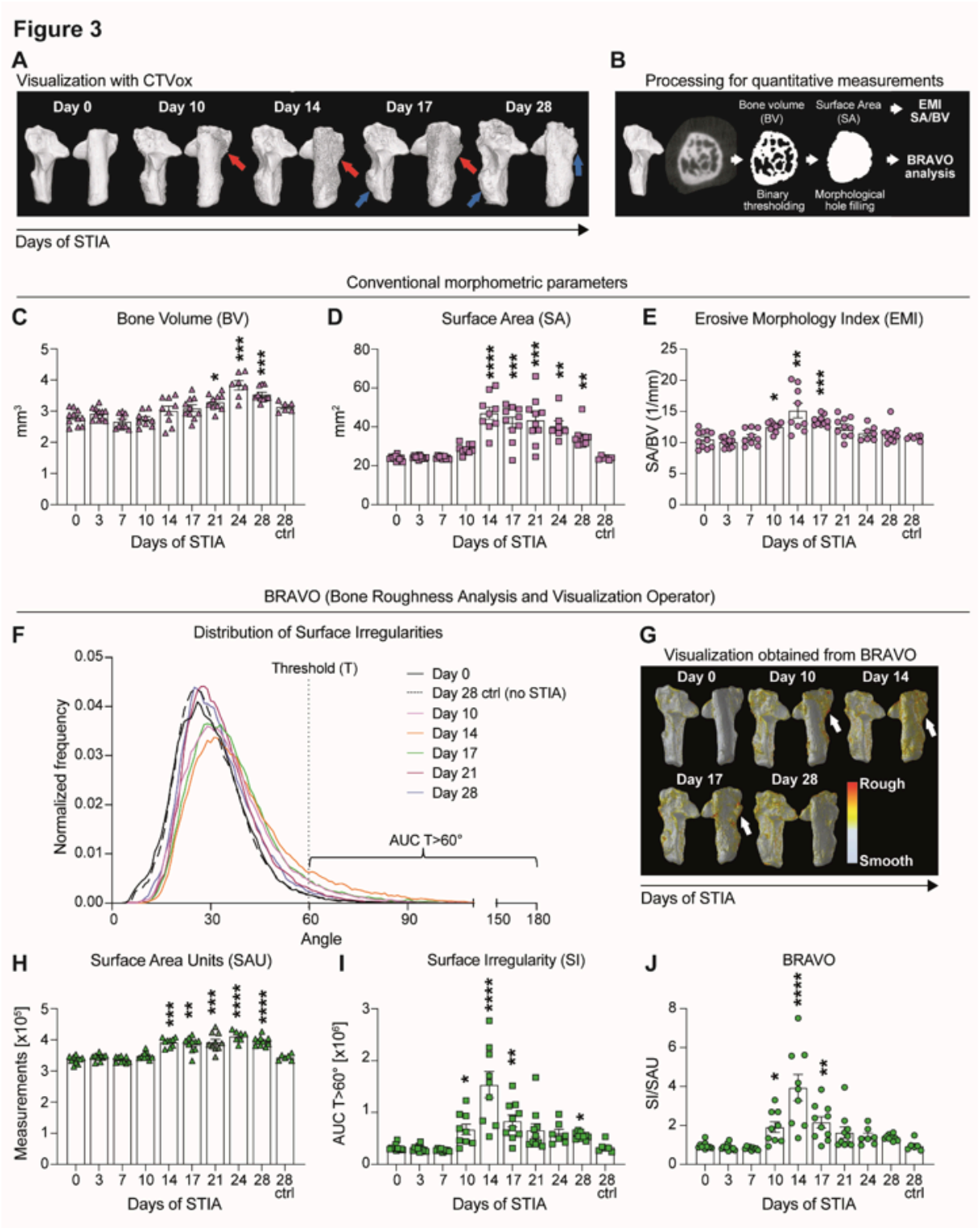


Figure 3

Quantitative µCT-based assessment of cortical bone remodeling during STIA using conventional morphometrics and the BRAVO-based workflow

A) Representative µCT images of the isolated calcaneus bone across selected time-point during STIA, illustrating changes in bone surface. Red arrows indicate area of bone erosions and blue arrows indicate

area of bone formation. Images generated using the CTVox software from Bruker. **B**) Representative image showing binary images (black and white) used to quantify Bone Volume (BV) and Surface Area (SA) in the isolated calcaneus. Bone volume is calculated on binary images obtained from binary thresholding and before morphological hole filling. Images after hole filling is used to calculate surface area. Analysis is performed in the CTAnalyzer software from Bruker. BRAVO values are calculated on binary images after morphological hole filling. See detailed description in Supplementary Material. **C**-**E**) Calculated measurements of bone volume, surface area and Erosive Morphology Index (EMI) across experimental time-points during STIA (n ≥ 7 per group; see Figure 1A; Day 28 no STIA controls n = 6 [Day 28 ctrl]). **F**) Distribution of local roughness across bone surfaces. Control samples (black) peak before 30°, whereas arthritic bones (colored) shift rightward with more values above the ~60° threshold, indicating increased bone irregularities. **G**) Heat maps generated from our BRAVO-workflow in MATLAB visualizing areas of increased surface roughness (red) during STIA. White arrows indicate areas of increased roughness (erosions). **H**,**I**) The BRAVO-derived measurements Surface Area Units (SAU) (**H**) and Surface Irregularities (SI) (**I**) during STIA. SI is calculated as the area under the curve of angles > 60° (n ≥ 7 per group, see Figure 1A, Day 28 ctrl n=6). **J**) BRAVO quantification of calcaneus based on normalizing the SI to SAU (SI/SAU) across experimental time-point during STIA (n ≥ 7 per group, see Figure 1A, Day 28 ctrl n=6). Each symbol in **C**,**D**,**E**,**H**,**I** and **J** represent an individual mouse. Bars represent means ± SEM. Statistical significance in **C**-**E**and **H**-**J** was determined by Kruskal-Wallis test followed by Dunn's multiple comparisons test, with each time-point compared to Day 0. **P*< 0.05, ***P* < 0.01, ****P* < 0.001, *****P* < 0.0001.

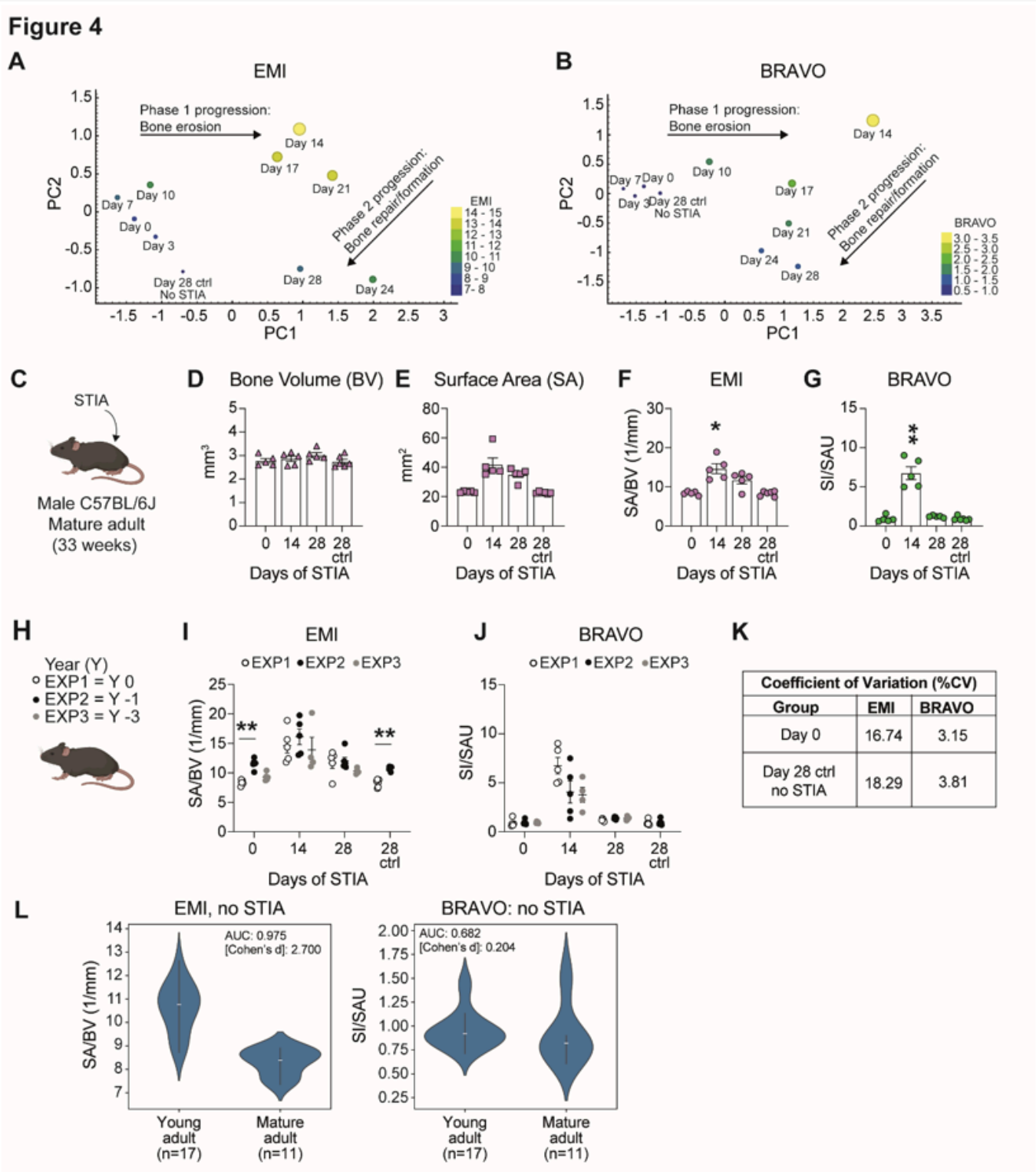


Figure 4

BRAVO provides age-stable and reproducible resolution of cortical bone remodeling during inflammatory arthritis

A,**B**) Principal Component Analysis (PCA) of EMI and BRAVO analysis. EMI PCA generated by integrating metrics of bone volume and bone surface and BRAVO PCA generated by integrating surface irregularities

and surface area units. **C**) Representative image of a 33-week-old male C57BL/6J mouse. **D**-**F**) Measurement of bone volume (BV), and surface area (SA) and EMI across different time-points during STIA (n ≥ 5 per group; see Supplementary Figure 4A). **G**) BRAVO-based quantification across different time-points during STIA (n ≥ 5 per group, see Supplementary Figure 4A). **H**) Representative images of three independent STIA experiments: EXP1 (performed in 2025; mice aged 33 weeks), EXP2 (2024; 12 weeks), and EXP3 (2022; 12 weeks). **I**-**J**) Average value of EMI and BRAVO from the three independent STIA experiments (EXP1-3) across 3 years (n ≥ 5 per EXP; see Figure 1A and Supplementary Figure 4A). **K**) %CV for EMI and BRAVO of non-arthritic (no STIA) mice on day 0 and day 28. **L**) Violin plots with embedded box plots showing BRAVO and EMI distributions in healthy non-arthritic (no STIA) young adult (12-16 weeks of age) and mature adult (33-37 weeks of age) mice (n ≥ 11 per group). For each comparison, group separability was quantified using the area under the ROC curve (AUC), defined as the probability that randomly selected sample is correctly ranked by the metric. Cohen's d was calculated as the standardized mean difference, defined as the difference between group means divided by the pooled standard deviation, describing how distinct the two groups are. Each symbol in **D**,**E**,**F**and **G** represents an individual mouse. Graphs represent means ± SEM. Statistical significance in **D-G**,**I** and **J** was determined by Kruskal-Wallis test followed by Dunn's multiple comparisons test, with each time-point compared to Day 0. *P < 0.05, **P < 0.01.

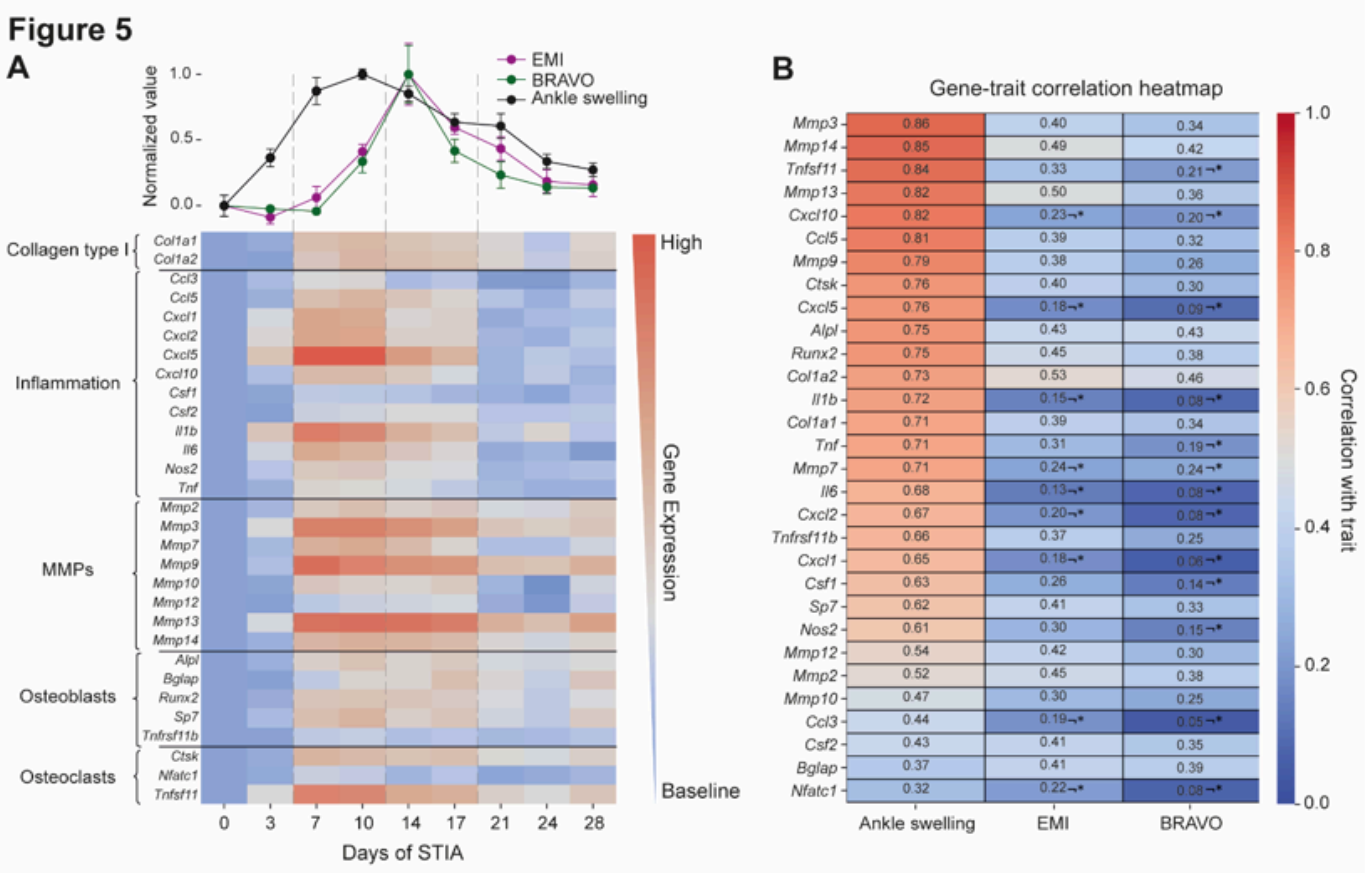


Figure 5

Kinetic joint transcriptional profiling links inflammatory and remodeling programs to clinical severity and structural bone changes during STIA

A) Time-course heatmap of gene expression showing mean ΔΔCt values per gene and time point (n ≥ 7 per group; see **Figure 1A**), with genes grouped according to predefined functional categories. Arthritis traits (ankle swelling, EMI, and BRAVO) are shown for reference. Gene expression was calculated as fold change relative to non-arthritic (no STIA) day 0 controls using the ΔΔCt method, normalizing the gene of interest to *Gapdh* (gene of interest - housekeeping gene). For visualization, sign-flipped values (−ΔΔCt) were plotted to show the increased expression corresponds to higher heatmap intensity. **B**) Gene-trait correlation heatmap showing spearman correlation coefficients between gene expression levels and individual arthritis traits. P-values were adjusted using the Benjamini-Hochberg false discovery rate (FDR) procedure. Correlations not significant after FDR correction (q ≥ 0.05) are marked with "¬*", whereas unlabeled cells indicate statistically significant associations.

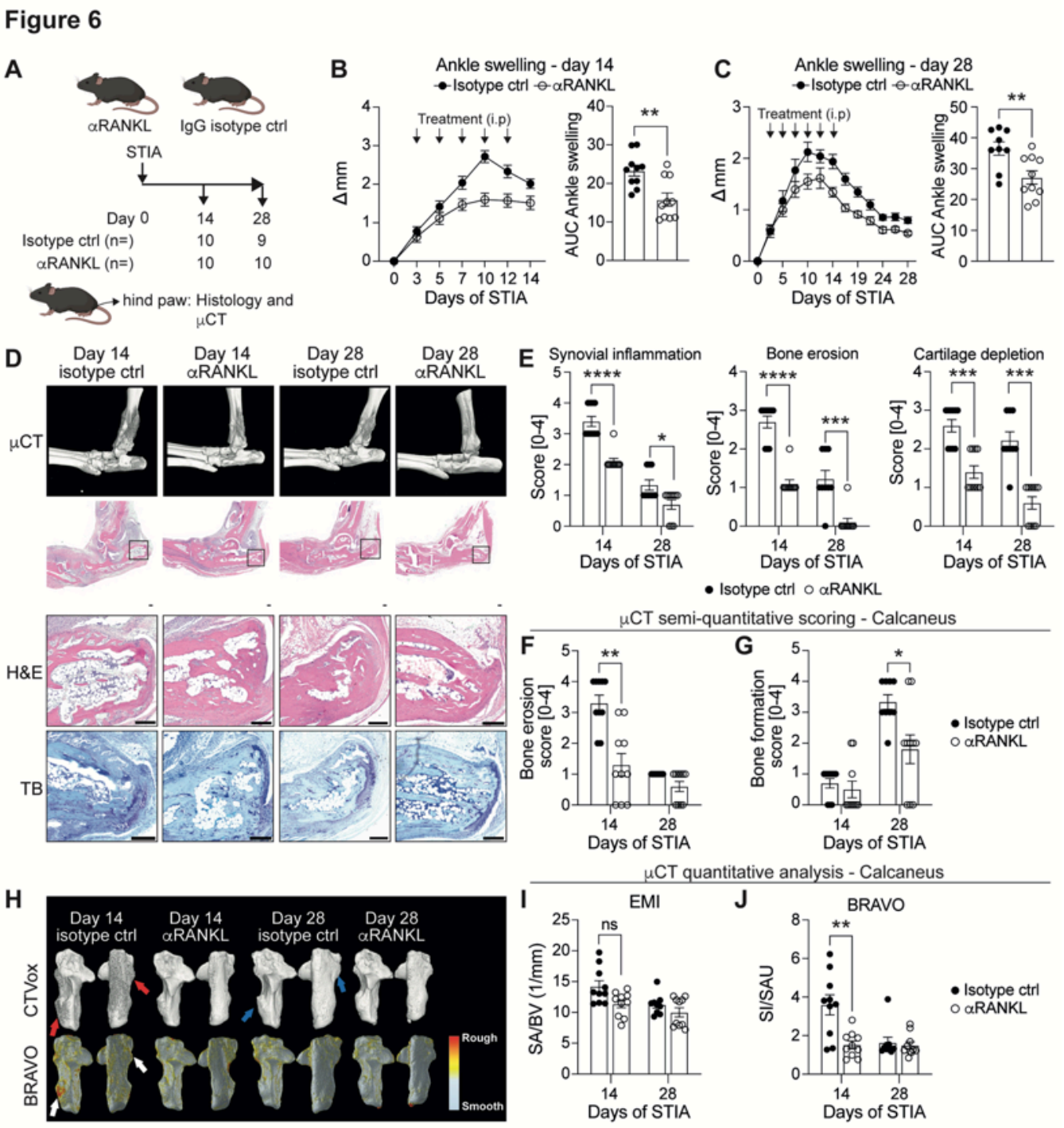


Figure 6

Surface roughness reveals treatment-induced attenuation of arthritis severity

A) Schematic overview of experimental set-up of treated mice (anti-RANKL [αRANKL] vs. IgG isotype ctrl) indicating time-points and collection of hind paws for further downstream analysis. N equals numbers of mice terminated per time-point. **B,C**) Ankle swelling comparing arthritis severity between αRANKL-treated and IgG isotype-treated mice during STIA progression of mice terminated either on day 14 or day 28, separately. Treatment started on day 3 after STIA induction. Mice terminated on day 14 received

treatment on days 3, 5, 7, 10 and 12, whereas mice terminated on day 28 received treatment on days 3,5,7,10, 12 and 14. Arrows indicate treatment with intraperitoneal (i.p). injection (n ≥ 9 per group, see **A**). Arthritis severity calculated using AUC. **D**,**E**) Representative µCT, H&E and TB images (**D**) used for histological analysis of synovial inflammation, bone erosion and cartilage depletion (**E**) in arthritic joints of αRANKL and IgG isotype-treated animals on day 14 and day 28 after STIA (n ≥ 9 per group, see **A**). Scale bars, 200 µm. **F**,**G**) Semi-quantitative scoring of bone erosion (**F**) and bone formation (**G)** of calcaneus between treatment groups at day 14 and day 28 after STIA (n ≥ 9 per group, see **A**). **H**) Representative µCT images of the calcaneus from αRANKL and IgG isotype-treated mice generated with either CTVox or obtained from our BRAVO-workflow. Red arrows indicating bone erosive area. Blue arrows indicating bone formative area. White arrows indicating areas of increased roughness (erosions). **I**,**J**) Quantitative assessment of µCT scans of the calcaneus from αRANKL or IgG isotype-treated mice at day 14 and day 28 after STIA using EMI (**I**) and BRAVO (**J**) (n ≥ 9 per group, see **A**). Graphs represent means ± SEM. Statistical significance in **B**,**C**,**E**,**G**,**I**and **J** was determined by Mann-Whitney. *P < 0.05, **P< 0.01, ***P < 0.001, ****P < 0.0001.

Supplementary Files

This is a list of supplementary files associated with this preprint. Click to download.

- SupplementaryBonesurfaceremodelingNguyenetal.docx